ACS APPLIED MATERIALS & INTERFACES

Research Article

Cite This: ACS Appl. Mater. Interfaces 2017, 9, 42912−42918

www.acsami.org

Few-Layer WSe_2 Schottky Junction-Based Photovoltaic Devices through Site-Selective Dual Doping

Seungpil Ko,[†] Junhong Na,[*,‡] Young-Sun Moon,[†] Ute Zschieschang,[‡] Rachana Acharya,[‡] Hagen Klauk,[‡] Gyu-Tae Kim,[†] Marko Burghard,[‡] and Klaus Kern[‡,§]

[†]School of Electrical Engineering, Korea University, 136-701 Seoul, Republic of Korea

[‡]Max-Planck-Institute for Solid State Research, Heisenbergstrasse 1, D-70569 Stuttgart, Germany

[§]Institut de Physique, École Polytechnique Fédérale de Lausanne, CH-1015 Lausanne, Switzerland

Supporting Information

ABSTRACT: Ultrathin sheets of two-dimensional (2D) materials like transition metal dichalcogenides have attracted strong attention as components of high-performance light-harvesting devices. Here, we report the implementation of Schottky junction-based photovoltaic devices through site-selective surface doping of few-layer WSe_2 in lateral contact configuration. Specifically, whereas the drain region is covered by a strong molecular p-type dopant (NDP-9) to achieve an Ohmic contact, the source region is coated with an Al_2O_3 layer, which causes local n-type doping and correspondingly an increase of the Schottky barrier at the contact. By scanning photocurrent microscopy using green laser light, it could be confirmed that photocurent generation is restricted to the region around the source contact. The local photoinduced charge separation is associated with a photoresponsivity of up to 20 mA W^{-1} and an external quantum efficiency of up to 1.3%. The demonstrated device concept should be easily transferrable to other van der Waals 2D materials.

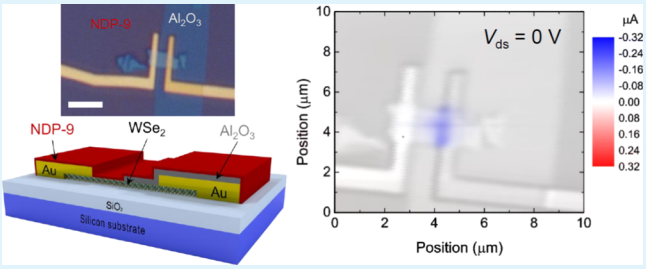

KEYWORDS: *tungsten diselenide, Schottky junction, photovoltaic, chemical doping, light harvesting*

INTRODUCTION

Ultrathin sheets of two-dimensional (2D) van der Waals materials are emerging as highly promising components of optoelectronic devices like photodetectors and photovoltaic devices.[1,2] Especially valuable materials for this purpose are transition metal dichalcogenides (TMDCs), which have been implemented into vertical as well as lateral device configurations. The vertical heterostructures combine either a p-type TMDC layer (e.g., $MoTe_2$) with an n-type TMDC layer (e.g., MoS_2)[3−6] or alternatively a TMDC layer with a semimetallic graphene layer.[7−11] Major advantages of these heterostructures are their stable, atomically sharp interfaces; their lack of surface dangling bonds; and the presence of strong light−matter interaction, leading to strong photon absorption.[11,12] Vertical p−n heterojunctions made of WSe_2/MoS_2,[4,13] $ReSe_2/MoS_2$,[14] MoS_2/WS_2,[15] or $WSe_2/MoSe_2$[6] have revealed excellent current rectification behavior and photoelectrical properties. Likewise, vertical Schottky junctions within a TMDC/graphene stack have been shown to exhibit notable photovoltaic performance.[7−11]

One type of lateral device configuration involves the implementation of a p−n junction into a TMDC layer by either local electrostatic or local chemical surface doping. Along these lines, electrostatic doping by buried gates has been used to create fully reconfigurable p−n junction diodes, thus enabling the observation of the photovoltaic effect in TMDC flakes.[16−21] More recently, photosensitive electrostatic p−n junctions have been realized by the electrolyte-gating technique, where cooling can be used to freeze the ion distribution.[22] Furthermore, lateral p−n junctions have been fabricated within TMDC layers through different chemical methods, including surface chemical doping[23,24] and lateral epitaxial growth.[25,26]

Another principal approach to lateral TMDC-based photovoltaic devices relies on the formation of a lateral Schottky contact between a TMDC and an appropriate metal electrode. It has been reported that the barrier height at the metal−TMDC interface, and correspondingly the local photoresponse, can be modulated by an applied gate voltage.[27−30] However, thus far only little work has been devoted to controlling the photoresponse at such interfaces by means of chemical doping. Here, we report the optoelectronic properties of Schottky junction-based photovoltaic devices wherein few-layer WSe_2 is oppositely doped in the vicinity of its source and drain contacts. WSe_2 is well-suited for the present purpose, as it exhibits ambipolar behavior in the transistor characteristics when contacted with common metal electrodes.[31,32] In photovoltaic devices, an ultrathin Al_2O_3 layer deposited near the source

Received: September 4, 2017
Accepted: November 22, 2017
Published: December 4, 2017

DOI: 10.1021/acsami.7b13395
ACS Appl. Mater. Interfaces 2017, 9, 42912−42918

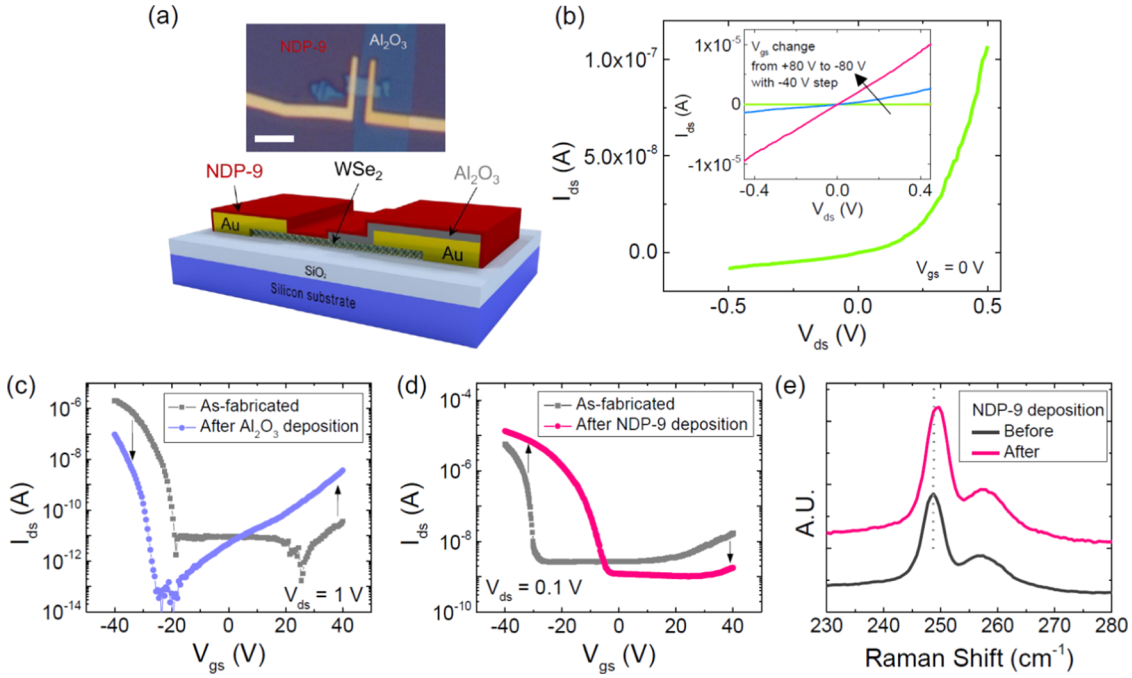

Figure 1. (a) Optical image (top) and schematic diagram (bottom) of a few-layer WSe_2 photovoltaic device. The scale bar in the optical image is 4 μm. (b) Output characteristic of the device at V_{gs} = 0 V. The inset shows the same data upon decreasing the gate voltage from +80 to −80 V by steps of −40 V. (c, d) Transfer characteristics of few-layer WSe_2 devices before and after (c) Al_2O_3 deposition and (d) NDP-9 deposition. (e) Raman spectra of a few-layer WSe_2 sheet before and after NDP-9 deposition.

electrode serves to increase the Schottky barrier height at this location. At the same time, deposition of a layer of strong p-type dopant NDP-9, which has previously been used to dope organic semiconductors,[33,34] near the drain electrode ensures that this contact becomes Ohmic. In this manner, effective light harvesting becomes possible even under global illumination of the entire device, whose channel length is on the order of several micrometers.

RESULTS AND DISCUSSION

Figure 1a shows an optical image (top) of a finalized, dual-doped few-layer WSe_2 device, together with a schematic representation of the device structure (bottom). The thickness of the few-layer WSe_2 sheet is about 7 nm, as determined by atomic force microscopy (see Supporting Information for more details). Details of the device fabrication process are provided in the Experimental Methods section. As apparent from Figure 1b, the output curve of the device recorded at zero gate voltage is nonlinear and asymmetric. This behavior is a first indication of asymmetric source and drain contacts. Moreover, as shown in the inset of Figure 1b, the application of a strongly negative gate voltage renders the output curve almost linear. The mechanism underlying this gate-induced change will be discussed below.

To confirm the doping effects of the two different types of dopant layers, the electrical properties of few-layer WSe_2 sheets were compared before and after deposition of the respective material onto the entire sheet. In the case of atomic layer deposition (ALD) of 20 nm Al_2O_3, the transfer characteristic experiences a shift toward negative gate voltages (see Figure 1c), signifying an n-doping effect. By comparison, deposition by thermal evaporation of 10 nm NDP-9 causes a shift of the transfer characteristic toward positive gate voltages (see Figure 1d), which is indicative of p-type doping. The p-doping by NDP-9 is further supported by the upshift of the $^1E_{2g}$ Raman peak visible in Figure 1e, which is in agreement with the observations made on other p-type dopants and distinguished from the downshift of this peak induced by n-type dopants.[35,36] Such downshift of the Raman peak was observed after Al_2O_3 deposition (see Figure S1), thus confirming the n-doping character in this case. Whereas the n-doping capability of Al_2O_3 for TMDCs most likely originates from positive trap charges in the oxide,[37−39] p-doping by the NDP-9 molecules can be explained by their strong electron acceptor property, similar to the mechanism operative in the case of organic semiconductors.[33,34]

In previous studies, surface dopants have been most often applied to few-layer TMDCs (with a sheet thickness of ∼10 nm).[36,40−42] However, it is noteworthy that the resulting doping degree depends on sheet thickness. Specifically, for thicknesses above ∼10 nm, the surface dopants and the back-gate voltage are not able to influence the entire body of the sheet because of the screening effect.[43,44] By comparison, although surface doping becomes fully effective in the case of monolayers, significant surface scattering and hence reduction of carrier mobility typically occur for such small thicknesses.[45] Accordingly, the present few-layer WSe_2 sheets can be considered as optimally suited for the surface doping approach.

To explore the spatially resolved photocurrent response of the devices, scanning photocurrent microscopy (SPCM) measurements were performed with a confocal microscope operating at λ = 514 nm. In Figure 2, where a zero-bias photocurrent map (acquired at V_{gs} = −40 V) is overlaid by an optical reflection image of the above device, photocurrent generation is seen to occur almost exclusively near the source contact. It is evident that the photocurrent ($I_{ph} = I_{ds,light} - I_{ds,dark}$) has a negative sign and reaches a significant magnitude on the order of −0.2 μA. The highly localized photocurrent

DOI: 10.1021/acsami.7b13395
ACS Appl. Mater. Interfaces 2017, 9, 42912−42918

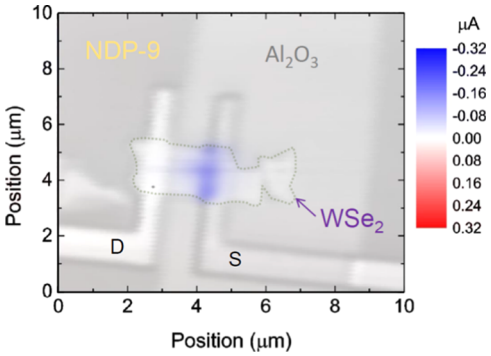

Figure 2. Scanning photocurrent microscopy (SPCM) map of a dual-doped few-layer WSe_2 device at room temperature. The map was recorded at V_{ds} = 0 V and V_{gs} = −40 V using a laser wavelength of 514 nm. Overlaid is the corresponding optical image of the device. The dotted line marks the WSe_2 sheet. "D" and "S" denote the drain and source electrodes, respectively.

strongly suggests the presence of a flat band situation (i.e., the presence of an Ohmic contact) at the drain electrode, whereas a Schottky barrier occurs at the source electrode, as indicated by the band diagrams in Figure 3a. This scenario, involving an increase (reduction) of the effective Schottky barrier induced by Al_2O_3 (NDP-9) as an n-type (p-type) dopant, is consistent with the previously reported effects of other surface chemical dopants.[31,36,46−49]

The influence of the drain−source voltage on the photoresponse of the device is apparent from the series of photocurrent maps shown in Figure 3a. The maps were recorded with three different values of the drain−source bias voltage (V_{ds}), specifically +100, 0, and −100 mV (in all cases V_{gs} = −40 V was applied). The magnitude of the negative photocurrent is seen to increase with increasingly negative drain−source voltage. This trend can be understood on the basis of the expected bias-induced changes of the band bending at the source contact, as outlined in the right panel of Figure 3a. In particular, for increasingly negative drain−source bias, the band bending associated with the Schottky barrier at the source electrode is expected to increase, whereas the bands at the drain contact should be only little affected.

The negative photocurrent generated upon illumination of the source contact region for V_{ds} = +200 mV is illustrated in Figure 3b as a function of gate voltage. For comparison, in Figure 3c the same transfer is plotted in a semilogarithmic manner. The negative photocurrent is observed with increasingly negative gate voltage, indicative of an increasing

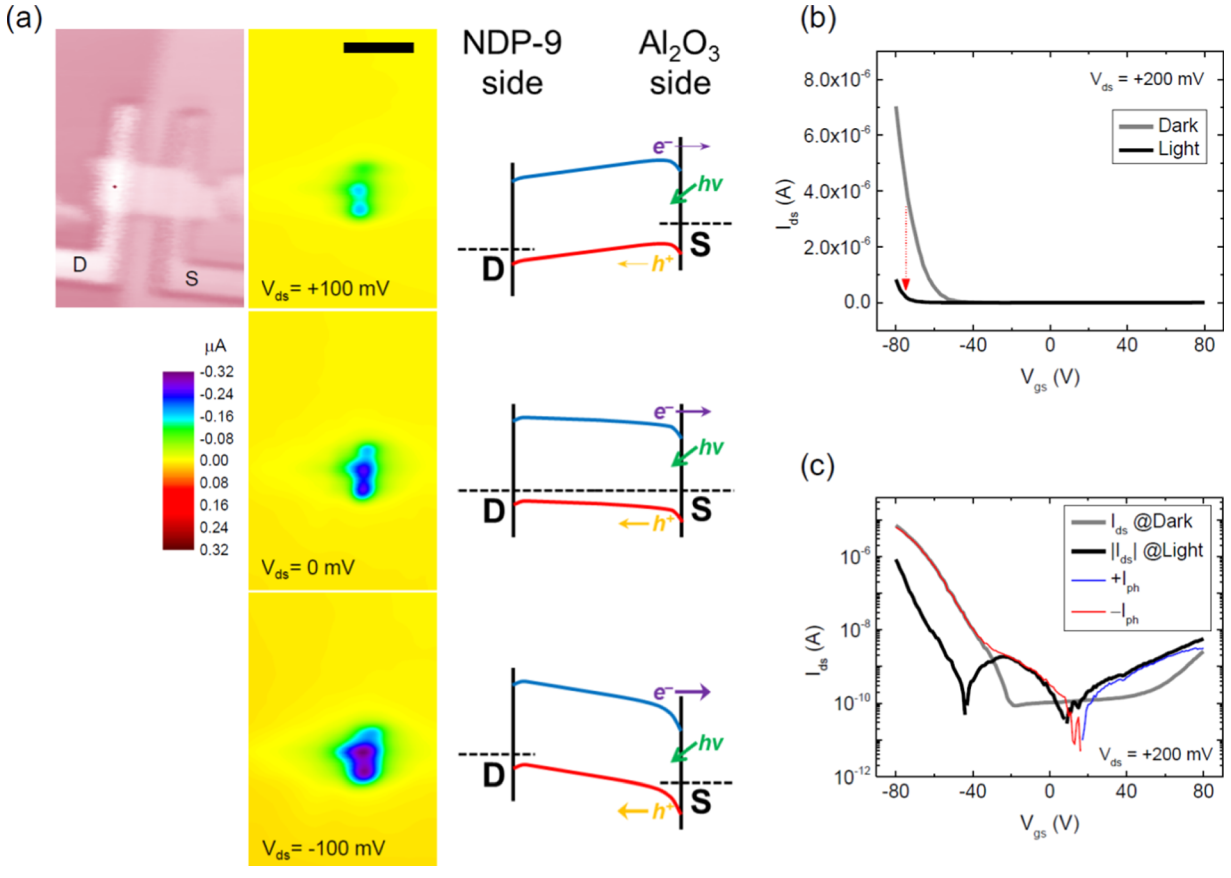

Figure 3. (a) Optical image of the device in Figure 2 (left) and the corresponding SPCM maps (middle) recorded at a drain−source voltage of +100, 0, and −100 mV, respectively. The scale bar is 2 μm. Band diagrams (right) for the corresponding drain−source bias conditions of the photocurrent maps. D and S denote the drain and source electrodes, respectively. (b) Transfer characteristics of the device with the linear current scale, acquired at V_{ds} = +200 mV in the dark and under local illumination at the WSe_2/source contact with a laser power of ∼300 μW. (c) Corresponding transfer characteristics of the same device with a logarithmic current scale, recorded at V_{ds} = +200 mV in the dark (gray) and under illumination (black). The blue and red curves show the difference between the black and gray curves as positive and negative photocurrents, respectively. To display the negative values on the logarithmic scale, the absolute values of the drain current under illumination and the negative sign of the negative photocurrent are plotted.

DOI: 10.1021/acsami.7b13395
ACS Appl. Mater. Interfaces 2017, 9, 42912−42918

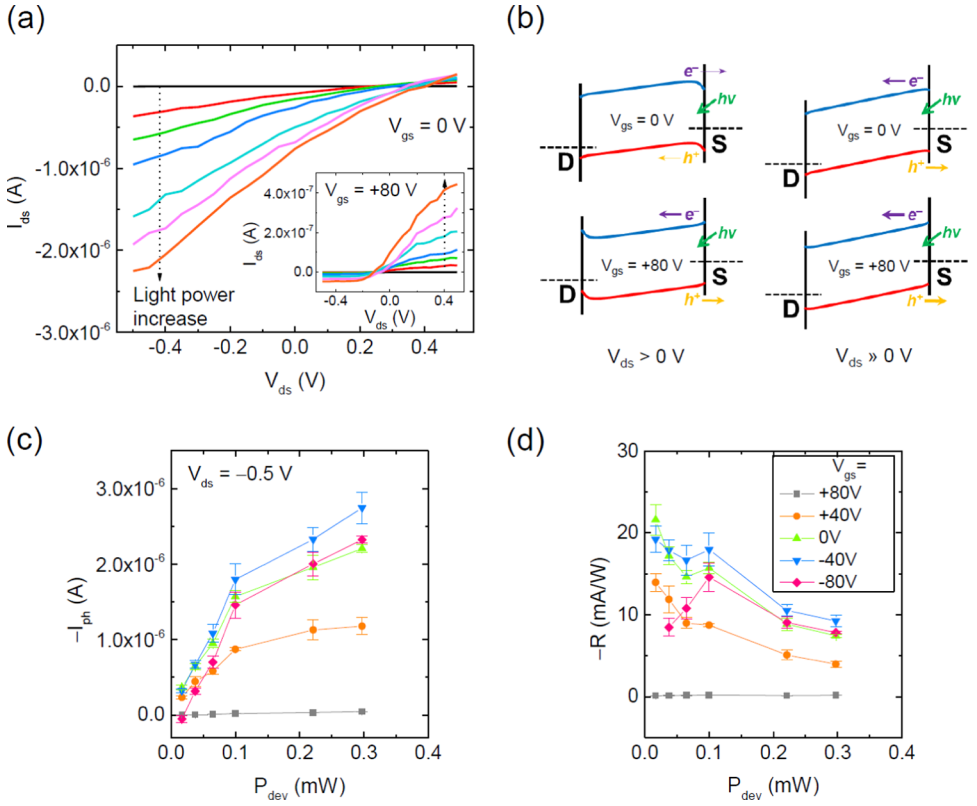

Figure 4. (a) Drain current vs drain voltage at V_{gs} = 0 V in the dark (black line) and under illumination with different laser powers of 16.9 μW (red), 37.5 μW (green), 65 μW (blue), 100 μW (cyan), 221 μW (pink), and 297 μW (orange). The device was illuminated at a WSe_2−source contact. The inset shows the corresponding output curves obtained with a gate voltage of +80 V. (b) Four band diagrams of the device at V_{gs} = 0 V (top) and +80 V (bottom) when V_{ds} > 0 V or $V_{ds} \gg 0$ V. (c) Photocurrent I_{ph} and (d) responsivity R as a function of laser power for local illumination at the WSe_2−source contact under V_{ds} = −0.5 V and five different gate voltages of +80, +40, 0, −40, and −80 V.

built-in electric field (enhanced band bending) at the source contact. Negative photocurrent generation prevailed in the general regime, that is, $V_{ds} \leq +100$ mV and $-80 \leq V_{gs} \leq +80$ V. Only for the largest positive drain−source and gate voltages, a positive photocurrent could be detected (see Figure 3c), demonstrating the principal possibility of inverting the band bending at the source contact.

Figure 4a displays the $I-V$ characteristics of the device recorded for different laser powers (λ = 514 nm) at gate voltages of V_{gs} = 0 V (main plot) and +80 V (inset). At V_{gs} = 0 V, increasing laser power leads to a pronounced increase of the drain−source current (negative photocurrent) for drain−source voltages below approximately +300 mV. Above this drain−source voltage, a positive photocurrent emerges, although its magnitude is quite small. At V_{gs} = +80 V, by contrast, a dominant positive photocurrent is observed above V_{ds} = 0 mV. The different behaviors at the two different gate voltages can be explained by the band diagrams in Figure 4b. For V_{gs} = 0 V in the drain−source bias regime of $0 < V_{ds} < +300$ mV (condition V_{ds} > 0 V on the left-hand side), the downward band bending at the source electrode and accordingly the negative photocurrent persist. However, when V_{ds} is increased above +300 mV (condition $V_{ds} \gg 0$ V on the right-hand side), inversion of the band bending and hence positive photocurrent occurs, as described above. In comparison, at V_{gs} = +80 V, the gate-induced Fermi level upshift in the few-layer WSe_2 decreases (increases) the Schottky barrier for the photogenerated hole (electron), thereby reversing the drift directions of the hole and the electron.

The dependence of the photocurrent and responsivity, $R = I_{ph}/P_{dev}$, of the device on laser power P_{dev} is shown in Figure 4c,d, respectively. As apparent from Figure 4c, the photocurrent recorded at V_{ds} = −0.5 V and at five different gate voltages increases close-to-linearly with increasing laser power up to approximately 0.1 mW. At the same time, the responsivity recorded at the same V_{ds} decreases with increasing laser power for all investigated gate voltages except V_{gs} = +80 V. The small responsivity detected for V_{gs} = +80 V reflects a low sensitivity ($I_{ds,light}/I_{ds,dark} \approx 1$), which arises from the significant dark current under this condition. In comparison, a significantly larger responsivity is found for smaller gate voltages, reaching a maximum value of 20 mA W^{-1} at V_{gs} = 0 and −40 V. It follows that through the combined effect of gate and drain−source voltages the device can be tuned between two different operation regimes, yielding photocurrents of opposite sign in the different drain−source bias windows.

The two different natures of the source and drain contacts on the few-layer WSe_2 enable one to operate the devices as light-harvesting elements. This is exemplified in Figure 5a,b, where for the above device, the $I-V$ curves before and after laser illumination with a power of 297 μW are depicted for V_{gs} = 0 and +80 V, respectively. The curves feature short-circuit current (I_{sc}) and open-circuit voltage (V_{oc}), from which the electrical power ($P_{el} = I_{ds} \cdot V_{ds}$) can be extracted. The values of the latter are shown in the respective insets of Figure 5a,b for the different laser powers. For V_{gs} = 0 V, a maximum electrical power of approximately 61 nW is found at V_{ds} = +0.16 V. The short-circuit current and open-circuit voltage as a function of

DOI: 10.1021/acsami.7b13395
ACS Appl. Mater. Interfaces 2017, 9, 42912−42918

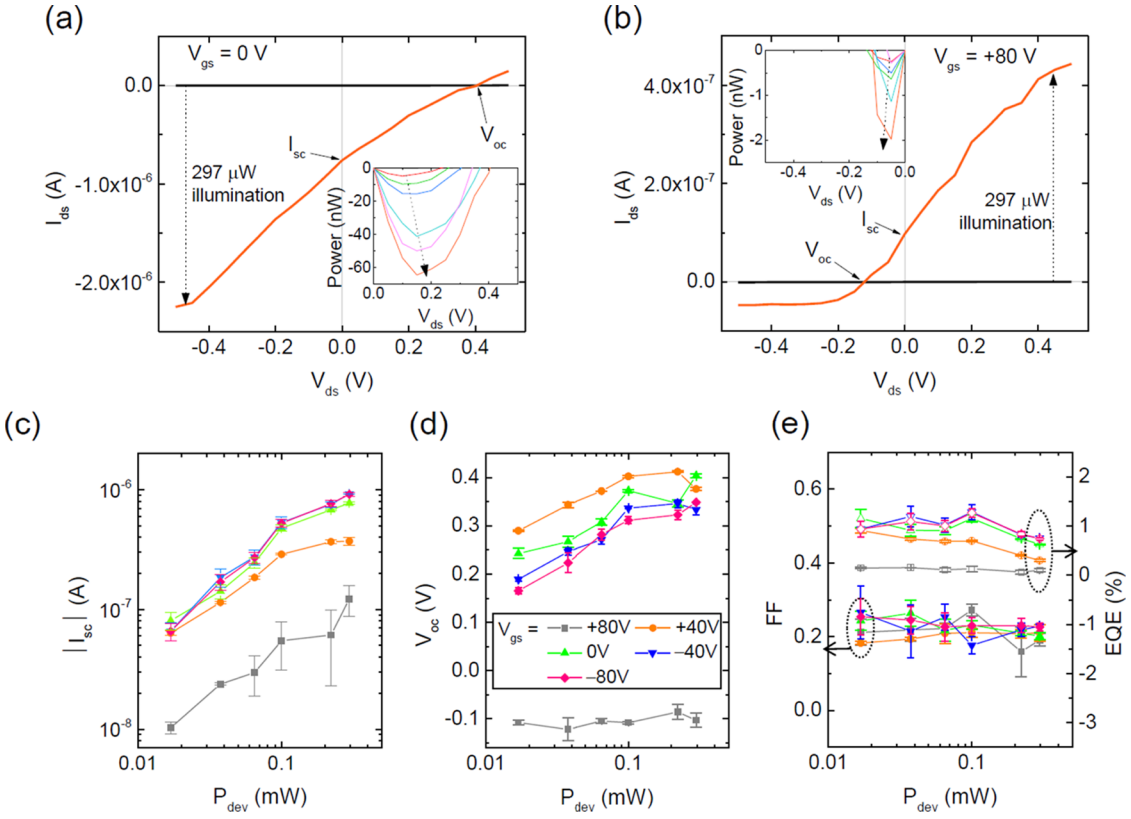

Figure 5. Drain current vs drain voltage in the dark and upon illumination with a laser power of 297 μW, acquired at V_{gs} = 0 (a) and +80 V (b). The insets show the drain−source voltage dependence of the electrical power derived from the short-circuit current (I_{sc}) and open-circuit voltage (V_{oc}) at V_{gs} = 0 and +80 V, respectively. I_{sc} (c), V_{oc} (d), and FF and EQE (filled and open symbols in (e), respectively) as a function of laser power at five different gate voltages of +80, +40, 0, −40, and −80 V.

laser power and gate voltage are presented in Figure 5c,d, respectively. In addition, the fill factor (FF = $P_{el}/(V_{oc}\cdot I_{sc})$) and external quantum efficiency (EQE = $I_{sc}/P_{dev}\cdot hc/(q\lambda)$, where h, c, q, and λ are the Planck constant, speed of light, electronic charge, and laser wavelength, respectively) are plotted as a function of laser power in Figure 5e. In an ideal photovoltaic cell, the short-circuit current and open-circuit voltage depend linearly and logarithmically on laser power, respectively. For the present device, with the exception of V_{gs} = +80 V, the short-circuit current (open-circuit voltage) indeed depends linearly (logarithmically) on the laser power up to 0.1 mW and then approaches saturation (see Figure 5c,d, respectively). The FF is largely independent of both, laser power and gate voltage, with a value of about 0.2. The maximum external quantum efficiency of 1.3% is reached already at relatively low laser powers. The EQE decrease in the high-laser-power regime is explainable by the saturation behaviors of I_{sc} and V_{oc} visible in Figure 5c,d. Possible explanations for this decrease comprise the optical absorption saturation in WSe_2, the screening of the built-in potential by excess carriers, or the increased electron−hole recombination by the increased interactions between the carriers.[5,8,50] For the power-conversion efficiency, defined as $\eta_{pv} = P_{el}/P_{dev}$, a maximum value of 0.03% was obtained. The maximum EQE of 1.3% is comparable to the values reported for vertical heterostructure-based devices such as WSe_2/black phosphorus p−n diodes[5] and about 1 order of magnitude larger than that of electrostatically defined WSe_2 p−n diodes.[19,20] By contrast, the maximum power-conversion efficiency of only 0.03% is well below the maximal values documented for electrostatic WSe_2 p−n diodes.[18,20] This difference arises from the low FF = 0.2 of the present devices, which is most likely due to parasitic resistances such as series and shunt resistances. The latter are manifested in the increasing slope at V_{ds} = 0 V in the I−V curves of Figure 4a with increasing laser power.[18,20] They may originate from, for instance, trap-induced carrier recombination loss or a low interface quality,[18,19] and it should be possible to reduce them, for instance, by annealing of the devices.

CONCLUSIONS

In summary, we have exploited site-selective doping of the electrical contact regions on few-layer WSe_2 sheets to obtain photovoltaic devices featuring a photoresponsivity of 20 mA W^{-1} and the external quantum efficiency of 1.3% at low bias. By SPCM investigation, we could verify that the p-doping by NDP-9 leads to a small built-in electric field at the source contact, whereas the n-doping by Al_2O_3 enhances the Schottky barrier at the drain contact. Thus, the realized Schottky junction-based photovoltaic devices are suitable for operation under global illumination. They reach an external quantum efficiency that is comparable to or better than that of vertical or lateral p−n junctions comprising WSe_2. It should be straightforward to implement the same device configuration also in other 2D semiconductors.

EXPERIMENTAL METHODS

The few-layer WSe_2 sheets were mechanically exfoliated from bulk crystals by the Scotch tape method onto highly doped silicon substrates coated with a thermally grown, 300 or 90 nm thick SiO_2 layer. Electrical contacts were defined on a few-layer-thick WSe_2 sheet

DOI: 10.1021/acsami.7b13395
ACS Appl. Mater. Interfaces 2017, 9, 42912−42918

by standard e-beam lithography, followed by in situ Ar plasma treatment, thermal evaporation of the Ti/Au (2/70 nm), and lift-off. For the devices in Figure 1c,d, this was followed by deposition of either a 20 nm thick Al_2O_3 layer by atomic layer deposition (ALD) (Cambridge Nanotech ALD system with $Al(CH_3)_3$ and H_2O as precursors at 100 °C at a base pressure of 10 mTorr) or a 10 nm thick NDP-9 layer by thermal evaporation, in both cases onto the entire substrate. For the Schottky junction-based photovoltaic devices, a second e-beam lithography step was used to define the area to selectively deposit the Al_2O_3 layer. After deposition of the 20 nm thick Al_2O_3 layer, lift-off was carried out in acetone, assisted by gentle ultrasonication. Subsequently, the NDP-9 layer was deposited on the entire substrate. Atomic force microscopy in tapping mode was used to determine the thickness of the sheets. Raman spectroscopy (λ_{exc} = 532 nm) was utilized to confirm that the few-layer WSe_2 sheets remained intact and to evaluate the effect of Al_2O_3 or NDP-9 deposition on the sheets.

All electrical transport and photocurrent measurements were carried out under ambient conditions. The electrical measurements were performed in direct current configuration using a Keithley 2400 source-meter and a Keithley 2000 multimeter. A confocal microscope (Leica TCS SP2, 50× objective lens with NA = 0.8) was used for the SPCM experiments, in which the samples were raster-scanned through the approximately 500 nm wide laser spot (linearly polarized light with λ = 514 nm).

■ ASSOCIATED CONTENT

Supporting Information

The Supporting Information is available free of charge on the ACS Publications website at DOI: 10.1021/acsami.7b13395.

Raman spectra resulted from Al_2O_3 deposition and atomic force microscopy on the few-layer WSe_2 devices (PDF)

■ AUTHOR INFORMATION

Corresponding Author

*E-mail: j.na@fkf.mpg.de.

ORCID

Junhong Na: 0000-0002-5314-2868

Notes

The authors declare no competing financial interest.

■ ACKNOWLEDGMENTS

The authors are grateful to the company Novaled for supplying the acceptor compound NDP-9. In addition, this research was supported by Nano·Material Technology Development Program through the National Research Foundation of Korea funded by Ministry of Science and ICT (NRF-2017M3A7B4049119) and under the framework of international cooperation program managed by the National Research Foundation of Korea (NRF-2016K2A9A2A14912825).

■ REFERENCES

(1) Dhanabalan, S. C.; Ponraj, J. S.; Zhang, H.; Bao, Q. Present perspectives of broadband photodetectors based on nanobelts, nanoribbons, nanosheets and the emerging 2D materials. *Nanoscale* **2016**, *8*, 6410−6434.

(2) Xia, F.; Wang, H.; Xiao, D.; Dubey, M.; Ramasubramaniam, A. Two-dimensional material nanophotonics. *Nat. Photonics* **2014**, *8*, 899−907.

(3) Zhang, K.; Zhang, T.; Cheng, G.; Li, T.; Wang, S.; Wei, W.; Zhou, X.; Yu, W.; Sun, Y.; Wang, P.; Zhang, D.; Zeng, C.; Wang, X.; Hu, W.; Fan, H. J.; Shen, G.; Chen, X.; Duan, X.; Chang, K.; Dai, N. Interlayer Transition and Infrared Photodetection in Atomically Thin Type-II $MoTe_2/MoS_2$ van der Waals Heterostructures. *ACS Nano* **2016**, *10*, 3852−3858.

(4) Sun, M.; Fang, Q.; Xie, D.; Sun, Y.; Xu, J.; Teng, C.; Dai, R.; Yang, P.; Li, Z.; Li, W.; Zhang, Y. Novel Transfer Behaviors in 2D MoS_2/WSe_2 Heterotransistor and Its Applications in Visible-Near Infrared Photodetection. *Adv. Electron. Mater.* **2017**, *3*, No. 1600502.

(5) Chen, P.; Zhang, T. T.; Zhang, J.; Xiang, J.; Yu, H.; Wu, S.; Lu, X.; Wang, G.; Wen, F.; Liu, Z.; Yang, R.; Shi, D.; Zhang, G. Gate tunable WSe_2-BP van der Waals heterojunction devices. *Nanoscale* **2016**, *8*, 3254−3258.

(6) Flöry, N.; Jain, A.; Bharadwaj, P.; Parzefall, M.; Taniguchi, T.; Watanabe, K.; Novotny, L. A $WSe_2/MoSe_2$ heterostructure photovoltaic device. *Appl. Phys. Lett.* **2015**, *107*, No. 123106.

(7) Gao, A.; Liu, E.; Long, M.; Zhou, W.; Wang, Y.; Xia, T.; Hu, W.; Wang, B.; Miao, F. Gate-tunable rectification inversion and photovoltaic detection in graphene/WSe_2 heterostructures. *Appl. Phys. Lett.* **2016**, *108*, No. 223501.

(8) Yu, W. J.; Liu, Y.; Zhou, H.; Yin, A.; Li, Z.; Huang, Y.; Duan, X. Highly efficient gate-tunable photocurrent generation in vertical heterostructures of layered materials. *Nat. Nanotechnol.* **2013**, *8*, 952−958.

(9) Luo, W.; Qin, S.; Long, M.; Liu, E.; Fu, Y.; Zhou, W.; Miao, F.; Zhang, S.; Zhang, R.; Zhang, X.-A. Tunable photoresponse with small drain voltage in few-layer graphene−WSe_2 heterostructures. *Phys. Lett. A* **2016**, *380*, 2575−2579.

(10) Zhang, W.; Chuu, C.-P.; Huang, J.-K.; Chen, C.-H.; Tsai, M.-L.; Chang, Y.-H.; Liang, C.-T.; Chen, Y.-Z.; Chueh, Y.-L.; He, J.-H.; Chou, M.-Y.; Li, L.-J. Ultrahigh-Gain Photodetectors Based on Atomically Thin Graphene-MoS_2 Heterostructures. *Sci. Rep.* **2014**, *4*, No. 3826.

(11) Britnell, L.; Ribeiro, R. M.; Eckmann, A.; Jalil, R.; Belle, B. D.; Mishchenko, A.; Kim, Y.-J.; Gorbachev, R. V.; Georgiou, T.; Morozov, S. V.; Grigorenko, A. N.; Geim, A. K.; Casiraghi, C.; Neto, A. H. C.; Novoselov, K. S. Strong Light-Matter Interactions in Heterostructures of Atomically Thin Films. *Science* **2013**, *340*, 1311−1314.

(12) Pant, A.; Mutlu, Z.; Wickramaratne, D.; Cai, H.; Lake, R. K.; Ozkan, C.; Tongay, S. Fundamentals of lateral and vertical heterojunctions of atomically thin materials. *Nanoscale* **2016**, *8*, 3870−3887.

(13) Cheng, R.; Li, D.; Zhou, H.; Wang, C.; Yin, A.; Jiang, S.; Liu, Y.; Chen, Y.; Huang, Y.; Duan, X. Electroluminescence and Photocurrent Generation from Atomically Sharp WSe_2/MoS_2 Heterojunction p−n Diodes. *Nano Lett.* **2014**, *14*, 5590−5597.

(14) Wang, X.; Huang, L.; Peng, Y.; Huo, N.; Wu, K.; Xia, C.; Wei, Z.; Tongay, S.; Li, J. Enhanced rectification, transport property and photocurrent generation of multilayer $ReSe_2/MoS_2$ p−n heterojunctions. *Nano Res.* **2016**, *9*, 507−516.

(15) Huo, N.; Kang, J.; Wei, Z.; Li, S.-S.; Li, J.; Wei, S.-H. Novel and Enhanced Optoelectronic Performances of Multilayer MoS_2−WS_2 Heterostructure Transistors. *Adv. Funct. Mater.* **2014**, *24*, 7025−7031.

(16) Wang, Z.; Wang, F.; Yin, L.; Huang, Y.; Xu, K.; Wang, F.; Zhan, X.; He, J. Electrostatically tunable lateral $MoTe_2$ p-n junction for use in high-performance optoelectronics. *Nanoscale* **2016**, *8*, 13245−13250.

(17) Memaran, S.; Pradhan, N. R.; Lu, Z.; Rhodes, D.; Ludwig, J.; Zhou, Q.; Ogunsolu, O.; Ajayan, P. M.; Smirnov, D.; Fernández-Domínguez, A. I.; García-Vidal, F. J.; Balicas, L. Pronounced Photovoltaic Response from Multilayered Transition-Metal Dichalcogenides PN-Junctions. *Nano Lett.* **2015**, *15*, 7532−7538.

(18) Pospischil, A.; Furchi, M. M.; Mueller, T. Solar-energy conversion and light emission in an atomic monolayer p-n diode. *Nat. Nanotechnol.* **2014**, *9*, 257−261.

(19) Baugher, B. W. H.; Churchill, H. O. H.; Yang, Y.; Jarillo-Herrero, P. Optoelectronic devices based on electrically tunable p-n diodes in a monolayer dichalcogenide. *Nat. Nanotechnol.* **2014**, *9*, 262−267.

(20) Groenendijk, D. J.; Buscema, M.; Steele, G. A.; Michaelis de Vasconcellos, S.; Bratschitsch, R.; van der Zant, H. S. J.; Castellanos-Gomez, A. Photovoltaic and Photothermoelectric Effect in a Double-Gated WSe_2 Device. *Nano Lett.* **2014**, *14*, 5846−5852.

DOI: 10.1021/acsami.7b13395
ACS Appl. Mater. Interfaces 2017, 9, 42912−42918

(21) Ross, J. S.; Klement, P.; Jones, A. M.; Ghimire, N. J.; Yan, J.; Mandrus, D. G.; Taniguchi, T.; Watanabe, K.; Kitamura, K.; Yao, W.; Cobden, D. H.; Xu, X. Electrically tunable excitonic light-emitting diodes based on monolayer WSe_2 p-n junctions. *Nat. Nanotechnol.* **2014**, *9*, 268−272.
(22) Kozawa, D.; Pu, J.; Shimizu, R.; Kimura, S.; Chiu, M.-H.; Matsuki, K.; Wada, Y.; Sakanoue, T.; Iwasa, Y.; Li, L.-J.; Takenobu, T. Photodetection in p−n junctions formed by electrolyte-gated transistors of two-dimensional crystals. *Appl. Phys. Lett.* **2016**, *109*, No. 201107.
(23) Lee, S. Y.; Kim, U. J.; Chung, J.; Nam, H.; Jeong, H. Y.; Han, G. H.; Kim, H.; Oh, H. M.; Lee, H.; Kim, H.; Roh, Y.-G.; Kim, J.; Hwang, S. W.; Park, Y.; Lee, Y. H. Large Work Function Modulation of Monolayer MoS_2 by Ambient Gases. *ACS Nano* **2016**, *10*, 6100−6107.
(24) Choi, M. S.; Qu, D.; Lee, D.; Liu, X.; Watanabe, K.; Taniguchi, T.; Yoo, W. J. Lateral MoS_2 p−n Junction Formed by Chemical Doping for Use in High-Performance Optoelectronics. *ACS Nano* **2014**, *8*, 9332−9340.
(25) Chen, K.; Wan, X.; Wen, J.; Xie, W.; Kang, Z.; Zeng, X.; Chen, H.; Xu, J.-B. Electronic Properties of MoS_2−WS_2 Heterostructures Synthesized with Two-Step Lateral Epitaxial Strategy. *ACS Nano* **2015**, *9*, 9868−9876.
(26) Duan, X.; Wang, C.; Shaw, J. C.; Cheng, R.; Chen, Y.; Li, H.; Wu, X.; Tang, Y.; Zhang, Q.; Pan, A.; Jiang, J.; Yu, R.; Huang, Y.; Duan, X. Lateral epitaxial growth of two-dimensional layered semiconductor heterojunctions. *Nat. Nanotechnol.* **2014**, *9*, 1024−1030.
(27) Zhang, W.; Chiu, M.-H.; Chen, C.-H.; Chen, W.; Li, L.-J.; Wee, A. T. S. Role of Metal Contacts in High-Performance Phototransistors Based on WSe_2 Monolayers. *ACS Nano* **2014**, *8*, 8653−8661.
(28) Li, H.-M.; Lee, D.-Y.; Choi, M. S.; Qu, D.; Liu, X.; Ra, C.-H.; Yoo, W. J. Metal-Semiconductor Barrier Modulation for High Photoresponse in Transition Metal Dichalcogenide Field Effect Transistors. *Sci. Rep.* **2014**, *4*, No. 4041.
(29) Fontana, M.; Deppe, T.; Boyd, A. K.; Rinzan, M.; Liu, A. Y.; Paranjape, M.; Barbara, P. Electron-hole transport and photovoltaic effect in gated MoS_2 Schottky junctions. *Sci. Rep.* **2013**, *3*, No. 1634.
(30) Yi, Y.; Wu, C.; Liu, H.; Zeng, J.; He, H.; Wang, J. A study of lateral Schottky contacts in WSe_2 and MoS_2 field effect transistors using scanning photocurrent microscopy. *Nanoscale* **2015**, *7*, 15711−15718.
(31) Jo, S.-H.; Kang, D.-H.; Shim, J.; Jeon, J.; Jeon, M. H.; Yoo, G.; Kim, J.; Lee, J.; Yeom, G. Y.; Lee, S.; Yu, H.-Y.; Choi, C.; Park, J.-H. A High-Performance WSe_2/h-BN Photodetector using a Triphenylphosphine (PPh_3)-Based n-Doping Technique. *Adv. Mater.* **2016**, *28*, 4824−4831.
(32) Das, S.; Appenzeller, J. WSe_2 field effect transistors with enhanced ambipolar characteristics. *Appl. Phys. Lett.* **2013**, *103*, No. 103501.
(33) Ante, F.; Kälblein, D.; Zschieschang, U.; Canzler, T. W.; Werner, A.; Takimiya, K.; Ikeda, M.; Sekitani, T.; Someya, T.; Klauk, H. Contact Doping and Ultrathin Gate Dielectrics for Nanoscale Organic Thin-Film Transistors. *Small* **2011**, *7*, 1186−1191.
(34) Zschieschang, U.; Kang, M. J.; Takimiya, K.; Sekitani, T.; Someya, T.; Canzler, T. W.; Werner, A.; Blochwitz-Nimoth, J.; Klauk, H. Flexible low-voltage organic thin-film transistors and circuits based on C10-DNTT. *J. Mater. Chem.* **2012**, *22*, 4273−4277.
(35) Kang, D.-H.; Shim, J.; Jang, S. K.; Jeon, J.; Jeon, M. H.; Yeom, G. Y.; Jung, W.-S.; Jang, Y. H.; Lee, S.; Park, J.-H. Controllable Nondegenerate p-Type Doping of Tungsten Diselenide by Octadecyltrichlorosilane. *ACS Nano* **2015**, *9*, 1099−1107.
(36) Chen, K.; Kiriya, D.; Hettick, M.; Tosun, M.; Ha, T.-J.; Madhvapathy, S. R.; Desai, S.; Sachid, A.; Javey, A. Air stable n-doping of WSe_2 by silicon nitride thin films with tunable fixed charge density. *APL Mater.* **2014**, *2*, No. 092504.
(37) Park, J. H.; Fathipour, S.; Kwak, I.; Sardashti, K.; Ahles, C. F.; Wolf, S. F.; Edmonds, M.; Vishwanath, S.; Xing, H. G.; Fullerton-Shirey, S. K.; Seabaugh, A.; Kummel, A. C. Atomic Layer Deposition of Al_2O_3 on WSe_2 Functionalized by Titanyl Phthalocyanine. *ACS Nano* **2016**, *10*, 6888−6896.
(38) Esposto, M.; Krishnamoorthy, S.; Nath, D. N.; Bajaj, S.; Hung, T.-H.; Rajan, S. Electrical properties of atomic layer deposited aluminum oxide on gallium nitride. *Appl. Phys. Lett.* **2011**, *99*, No. 133503.
(39) Na, J.; Joo, M.-K.; Shin, M.; Huh, J.; Kim, J.-S.; Piao, M.; Jin, J. E.; Jang, H.-K.; Choi, H. J.; Shim, J. H.; Kim, G. T. Low-Frequency Noise in Multilayer MoS_2 Field-Effect Transistors: The Effect of High-k Passivation. *Nanoscale* **2014**, *6*, 433−441.
(40) Ryu, M.-Y.; Jang, H.-K.; Lee, K. J.; Piao, M.; Ko, S.-P.; Shin, M.; Huh, J.; Kim, G.-T. Triethanolamine doped multilayer MoS_2 field effect transistors. *Phys. Chem. Chem. Phys.* **2017**, *19*, 13133−13139.
(41) Wang, G.; Bao, L.; Pei, T.; Ma, R.; Zhang, Y.-Y.; Sun, L.; Zhang, G.; Yang, H.; Li, J.; Gu, C.; Du, S.; Pantelides, S. T.; Schrimpf, R. D.; Gao, H.-J. Introduction of Interfacial Charges to Black Phosphorus for a Family of Planar Devices. *Nano Lett.* **2016**, *16*, 6870−6878.
(42) Kiriya, D.; Tosun, M.; Zhao, P.; Kang, J. S.; Javey, A. Air-Stable Surface Charge Transfer Doping of MoS_2 by Benzyl Viologen. *J. Am. Chem. Soc.* **2014**, *136*, 7853−7856.
(43) Liu, Y.; Guo, J.; He, Q.; Wu, H.; Cheng, H.-C.; Ding, M.; Shakir, I.; Gambin, V.; Huang, Y.; Duan, X. Vertical Charge Transport and Negative Transconductance in Multilayer Molybdenum Disulfides. *Nano Lett.* **2017**, *17*, 5495−5501.
(44) Li, H.-M.; Lee, D.; Qu, D.; Liu, X.; Ryu, J.; Seabaugh, A.; Yoo, W. J. Ultimate thin vertical p−n junction composed of two-dimensional layered molybdenum disulfide. *Nat. Commun.* **2015**, *6*, No. 6564.
(45) Li, S.-L.; Wakabayashi, K.; Xu, Y.; Nakaharai, S.; Komatsu, K.; Li, W.-W.; Lin, Y.-F.; Aparecido-Ferreira, A.; Tsukagoshi, K. Thickness-Dependent Interfacial Coulomb Scattering in Atomically Thin Field-Effect Transistors. *Nano Lett.* **2013**, *13*, 3546−3552.
(46) Zhou, C.; Zhao, Y.; Raju, S.; Wang, Y.; Lin, Z.; Chan, M.; Chai, Y. Carrier Type Control of WSe_2 Field-Effect Transistors by Thickness Modulation and MoO_3 Layer Doping. *Adv. Funct. Mater.* **2016**, *26*, 4223−4230.
(47) Wi, S.; Chen, M.; Li, D.; Nam, H.; Meyhofer, E.; Liang, X. Photovoltaic response in pristine WSe_2 layers modulated by metal-induced surface-charge-transfer doping. *Appl. Phys. Lett.* **2015**, *107*, No. 062102.
(48) Zhao, P.; Kiriya, D.; Azcatl, A.; Zhang, C.; Tosun, M.; Liu, Y.-S.; Hettick, M.; Kang, J. S.; McDonnell, S.; Kc, S.; Guo, J.; Cho, K.; Wallace, R. M.; Javey, A. Air Stable p-Doping of WSe_2 by Covalent Functionalization. *ACS Nano* **2014**, *8*, 10808−10814.
(49) Fang, H.; Chuang, S.; Chang, T. C.; Takei, K.; Takahashi, T.; Javey, A. High-Performance Single Layered WSe_2 p-FETs with Chemically Doped Contacts. *Nano Lett.* **2012**, *12*, 3788−3792.
(50) Massicotte, M.; Schmidt, P.; Vialla, F.; Schädler, K. G.; Reserbat Plantey, A.; Watanabe, K.; Taniguchi, T.; Tielrooij, K. J.; Koppens, F. H. L. Picosecond photoresponse in van der Waals heterostructures. *Nat. Nanotechnol.* **2016**, *11*, 42−46.

DOI: 10.1021/acsami.7b13395
ACS Appl. Mater. Interfaces 2017, 9, 42912−42918

Supporting Information

Few-layer WSe_2 Schottky junction-based photovoltaic devices through site-selective dual doping

Seungpil Ko[a], Junhong Na[b,], Young-Sun Moon[a], Ute Zschieschang[b], Rachana Acharya[b], Hagen Klauk[b], Gyu-Tae Kim[a], Marko Burghard[b], and Klaus Kern[b,c]*

[a]School of Electrical Engineering, Korea University, Seoul 136-701, Republic of Korea

[b]Max-Planck-Institute for Solid State Research, Heisenbergstrasse 1, D-70569 Stuttgart, Germany

[c]Institut de Physique, École Polytechnique Fédérale de Lausanne, CH-1015 Lausanne, Switzerland

[*]Corresponding Author E-mail: j.na@fkf.mpg.de

Al_2O_3 deposition effect on Raman spectra of few-layer WSe_2 sheet

The transfer characteristics before and after the Al_2O_3 deposition in Figure 1(d) of the main text were taken as evidence for the n-type doping effect of the Al_2O_3 deposition on the few-layer WSe_2 sheet. We used confocal Raman spectroscopy to confirm this effect.[1-5] In contrast to the upshift of the $E_{2g}{}^1$ Raman peak due to the NDP-9 induced p-type doping as shown in Figure 1(e) of the main text,[4] we observed a downshift (~0.5 cm^{-1}) of this peak after the Al_2O_3 deposition, as shown in Figure S1. The downshift underlines the n-doping character of Al_2O_3 and is in agreement with the effect of other n-type dopants such as silicon nitride.[3]

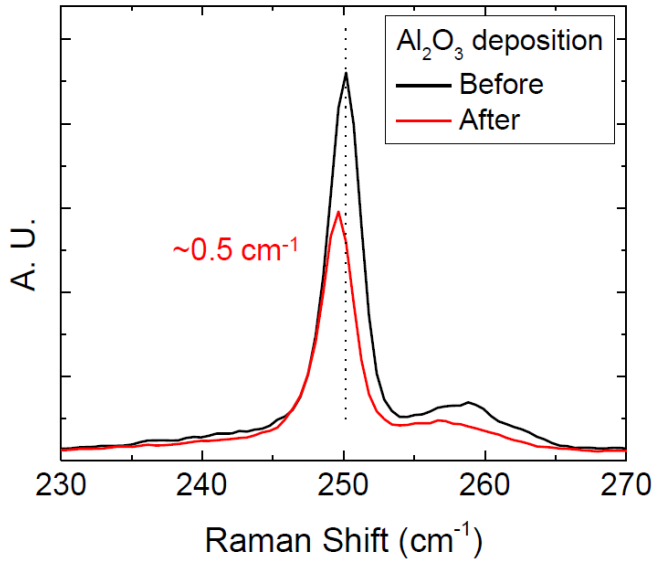

Figure S1. Raman spectra of a few-layer WSe_2 sheet (~5 nm thick) before and after the Al_2O_3 passivation. The peak at ~250 cm^{-1} experiences a downshift by ~0.5 cm^{-1} due to the oxide deposition.

Atomic force microscopy on few-layer WSe_2 devices

Figure S2 shows the topographic image of the few-layer WSe_2 device in the main text measured by atomic force microscopy. The height profile along the white line in Figure S1(a), as depicted in Figure S1(b), reveals a thickness of ~ 7 nm for the few-layer WSe_2 sheet.

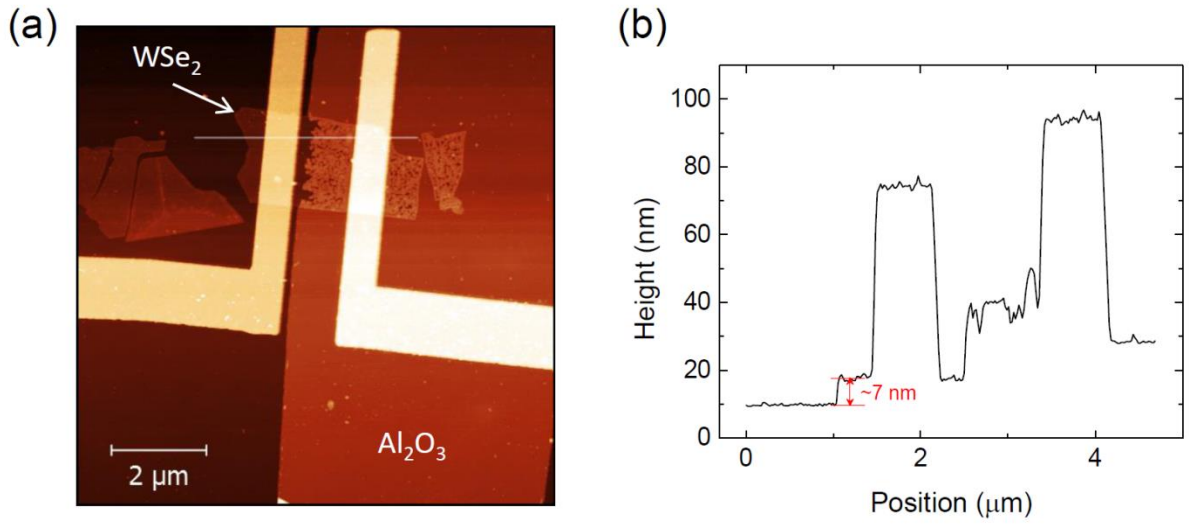

Figure S2. (a) A topographic image of the few-layer WSe_2 device measured by atomic force microscopy. (b) Height profile along the white line in panel (a). The thickness of the few-layer WSe_2 sheet is determined to be ~7 nm.

The AFM section profile furthermore confirms the presence of a ~20 nm thick Al_2O_3 layer. It should be noted that, in contrast to the uniformly deposited Al_2O_3 on the SiO_2 and metal electrodes, the Al_2O_3 film is less regular in the region of the few-layer WSe_2 sheet. The same phenomenon has been observed on another few-layer WSe_2 device (see Figure S3). The latter observation is understandable from the fact that 2-dimensional (2D) van der Waals materials including WSe_2 have only few surface sites for the chemisorption of the atomic layer deposition (ALD) precursors.[6-12] The uniformity of the ALD-grown Al_2O_3 film on 2D materials can be

improved by controlling the growth temperature of the film, surface functionalization, insertion of buffer layer, and so on.[6-10, 12] An interesting observation in this context is the formation of a uniform Al_2O_3 film on the few-layer WSe_2 sheet near the edge of the metal electrode, as apparent from Figure S2(a) and S3(b). This finding points toward the presence of a higher density of nucleation sites, such that the ALD process yields dense coverage. Importantly, the uniformly deposited Al_2O_3 film near one metal electrode is sufficient to partially n-dope the few-layer WSe_2, which is essential for the observed Schottky junction-based photovoltaic effect.

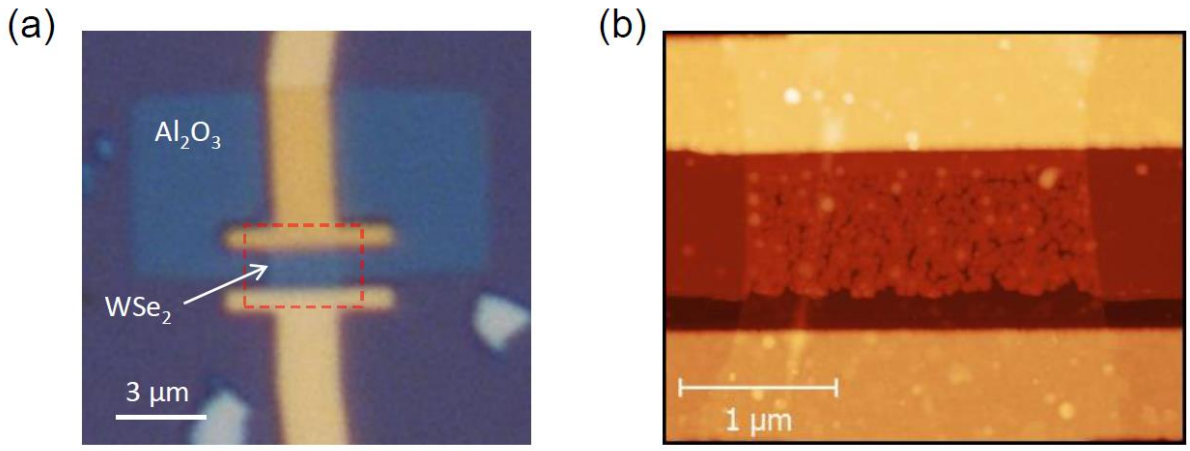

Figure S3. (a) An optical image of another few-layer WSe_2 device. (b) Corresponding topographic AFM image taken from the dashed rectangular region in panel (a). Uniform Al_2O_3 film formation on the few-layer WSe_2 sheet has occurred near the edge of the metal electrode.

REFERENCES

(1) Shi, Y.; Huang, J.-K.; Jin, L.; Hsu, Y.-T.; Yu, S. F.; Li, L.-J.; Yang, H. Y. Selective Decoration of Au Nanoparticles on Monolayer MoS_2 Single Crystals. *Sci. Rep.* **2013,** *3*, 1839.

(2) Ryu, M.-Y.; Jang, H.-K.; Lee, K. J.; Piao, M.; Ko, S.-P.; Shin, M.; Huh, J.; Kim, G.-T. Triethanolamine doped multilayer MoS_2 field effect transistors. *Phys. Chem. Chem. Phys.* **2017,** *19*, 13133-13139.

(3) Chen, K.; Kiriya, D.; Hettick, M.; Tosun, M.; Ha, T.-J.; Madhvapathy, S. R.; Desai, S.; Sachid, A.; Javey, A. Air stable n-doping of WSe_2 by silicon nitride thin films with tunable fixed charge density. *APL Mater.* **2014,** *2*, 092504.

(4) Kang, D.-H.; Shim, J.; Jang, S. K.; Jeon, J.; Jeon, M. H.; Yeom, G. Y.; Jung, W.-S.; Jang, Y. H.; Lee, S.; Park, J.-H. Controllable Nondegenerate p-Type Doping of Tungsten Diselenide by Octadecyltrichlorosilane. *ACS Nano* **2015,** *9*, 1099-1107.

(5) Kiriya, D.; Tosun, M.; Zhao, P.; Kang, J. S.; Javey, A. Air-Stable Surface Charge Transfer Doping of MoS_2 by Benzyl Viologen. *J. Am. Chem. Soc.* **2014,** *136*, 7853-7856.

(6) Park, T.; Kim, H.; Leem, M.; Ahn, W.; Choi, S.; Kim, J.; Uh, J.; Kwon, K.; Jeong, S.-J.; Park, S.; Kim, Y.; Kim, H. Atomic layer deposition of Al_2O_3 on MoS_2, WS_2, WSe_2, and h-BN: surface coverage and adsorption energy. *RSC Advances* **2017,** *7*, 884-889.

(7) Azcatl, A.; Wang, Q.; Kim, M. J.; Wallace, R. M. Al_2O_3 on WSe_2 by ozone based atomic layer deposition: Nucleation and interface study. *APL Mater.* **2017,** *5*, 086108.

(8) Park, J. H.; Fathipour, S.; Kwak, I.; Sardashti, K.; Ahles, C. F.; Wolf, S. F.; Edmonds, M.; Vishwanath, S.; Xing, H. G.; Fullerton-Shirey, S. K.; Seabaugh, A.; Kummel, A. C. Atomic Layer Deposition of Al_2O_3 on WSe_2 Functionalized by Titanyl Phthalocyanine. *ACS Nano* **2016,** *10*, 6888-6896.

(9) Shokouh, S. H. H.; Jeon, P. J.; Pezeshki, A.; Choi, K.; Lee, H. S.; Kim, J. S.; Park, E. Y.; Im, S. High-Performance, Air-Stable, Top-Gate, p-Channel WSe_2 Field-Effect Transistor with Fluoropolymer Buffer Layer. *Adv. Funct. Mater.* **2015,** *25*, 7208-7214.

(10) Cheng, L.; Qin, X.; Lucero, A. T.; Azcatl, A.; Huang, J.; Wallace, R. M.; Cho, K.; Kim, J. Atomic Layer Deposition of a High-k Dielectric on MoS_2 Using Trimethylaluminum and Ozone. *ACS Appl. Mater. Interfaces* **2014,** *6*, 11834-11838.

(11) McDonnell, S.; Brennan, B.; Azcatl, A.; Lu, N.; Dong, H.; Buie, C.; Kim, J.; Hinkle, C. L.; Kim, M. J.; Wallace, R. M. HfO_2 on MoS_2 by Atomic Layer Deposition: Adsorption Mechanisms and Thickness Scalability. *ACS Nano* **2013,** *7*, 10354-10361.

(12) Liu, H.; Xu, K.; Zhang, X.; Ye, P. D. The integration of high-k dielectric on two-dimensional crystals by atomic layer deposition. *Appl. Phys. Lett.* **2012,** *100*, 152115.